POLITECNICO DI TORINO
Repository ISTITUZIONALE

Dissipative and thermal aspects in cyclic loading of additive manufactured AISI 316L

Original
Dissipative and thermal aspects in cyclic loading of additive manufactured AISI 316L / Santoro, L., Sesana, R., Diller, J., Radlbeck, C., Mensinger, M.. - In: ENGINEERING FAILURE ANALYSIS. - ISSN 1350-6307. - 163:A(2024). [10.1016/j.engfailanal.2024.108446]

Availability:
This version is available at: 11583/2988863 since: 2024-05-20T11:15:36Z

Publisher:
Elsevier

Published
DOI:10.1016/j.engfailanal.2024.108446

Terms of use:

This article is made available under terms and conditions as specified in the corresponding bibliographic description in the repository

Publisher copyright

(Article begins on next page)

16 November 2026

Engineering Failure Analysis 163 (2024) 108446

Contents lists available at ScienceDirect

Engineering Failure Analysis

journal homepage: www.elsevier.com/locate/engfailanal

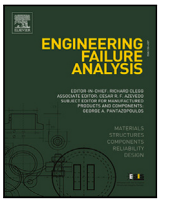

Dissipative and thermal aspects in cyclic loading of additive manufactured AISI 316L

Luca Santoro [a,*], Raffaella Sesana [a], Johannes Diller [b], Christina Radlbeck [b], Martin Mensinger [b]

[a] Dipartimento di Ingegneria Meccanica e Aerospaziale - Politecnico di Torino, Corso Duca degli Abruzzi 24, Torino, 10129, Italy
[b] Technical University of Munich, TUM School of Engineering and Design, Chair of Metal Structures, Arcisstraße 21, Munich, 80333, Germany

ARTICLE INFO

Keywords:
Additive manufacturing
Fatigue
Thermography
Micro-shakedown
Intrinsic dissipation

ABSTRACT

This study presents a comprehensive understanding of the fatigue behavior of 316L stainless steel specimens produced using the laser powder bed fusion (PBF-LB/M) method. The investigation has been conducted through a multifaceted approach that includes surface roughness analysis, density measurements, microstructural examination, fatigue testing, strain measurements, and thermographic analysis. Thermographic data processing models, i.e. the bi-power law (TCM-modified) model and the TCM method, are applied to fatigue test results of standard samples to evaluate fatigue limit values. The fatigue limit of the samples was estimated using the Murakami Method (MM), Constant Amplitude Loading (CAL) and Step Loading (SL) tests. The proposed methodology allows exploration of the entire stress level range within a single test, which could allow evaluation of the fatigue limit of components within only one test. This study is the starting point for a rapid evaluation method for estimating the fatigue limit using thermography, offering a cost-effective, time-efficient, and non-destructive means of assessing the fatigue performance of materials produced using additive manufacturing processes.

1. Introduction

The study of high-cycle fatigue in materials, particularly metals, has been a focal point of research for many years. This research has often been associated with the analysis of the classical fatigue curve (S-N curve), which is linked to the study of dissipative phenomena in materials subjected to cyclic loadings and the corresponding variation of physical parameters such as energy dissipation [1]. While in the so-called 'low cycle fatigue' damaging phenomena involve all the volume, being easier to model and measure, in the high cycle fatigue the microplastic and microcracking phenomena are stochastically activated. To this aim, the thermographic approach represents a reliable method to study the damaging phenomena.

In recent decades, the focus has shifted towards establishing a multiscale approach. This approach aims to connect the macroscopic damage of a structure subjected to cyclic loading and the corresponding irreversible mechanisms at the grain scale. These mechanisms are related to the variation of dissipative parameters and are associated with the gliding of dislocations and the creation of slip bands [2]. Generally speaking, this aspect is neglected when the material is underloaded in his elastic field, in fact, dislocation phenomena does not happen in the whole volume but are statistically locally activated.

These damaging phenomena can be satisfactorily described from both a theoretical and an experimental point of view by intrinsic dissipation, which is a direct consequence of the irreversible mechanism. Intrinsic dissipation, expressed in terms of heat dissipation,

* Corresponding author.
E-mail addresses: luca.santoro@polito.it (L. Santoro), raffaella.sesana@polito.it (R. Sesana), johannes.diller@tum.de (J. Diller), c.radlbeck@tum.de (C. Radlbeck), mensinger@tum.de (M. Mensinger).

https://doi.org/10.1016/j.engfailanal.2024.108446
Received 23 February 2024; Received in revised form 13 May 2024; Accepted 13 May 2024
Available online 17 May 2024
1350-6307/© 2024 The Author(s). Published by Elsevier Ltd. This is an open access article under the CC BY-NC-ND license (http://creativecommons.org/licenses/by-nc-nd/4.0/).

Nomenclature

$\Delta(\Sigma_0)$	Global microplasticization dissipated energy density in a cycle (J m^{-3})
φ	Lazan's loss angle, phase angle between stress and strain (rad)
ζ	Damping constant (MPa^{1-n})
ρ	Mass density (kg/m^3)
θ	Specimen surface temperature (K or °C)
$\tilde{\theta}$	Mean superficial thermal increment during a load cycle (K or °C)
$\dot{\tilde{\theta}}$	Time derivative of specimen surface temperature, average on a loading cycle (K s^{-1})
$\overline{\theta}$	Stabilization superficial thermal increment
ω_r	Loading pulsation (rad/s)
Ω_0	Strain amplitude in cyclic fatigue loading (m/m)
Σ_0	Stress amplitude in cyclic fatigue loading (MPa)
ηV_0	Term describing thermal process kinetic (K mm^3 MPa^{-2})
σ_d	Fatigue limit (MPa)
τ_{eq}	Time constant ()
A_h	Hysteresis loop area (J m^{-3})
AM	Additive manufacturing
a_M	Murakami defect depth (μm)
c	Specific heat (J Kg^{-1} K^{-1})
D	Lazan's damping energy, unit energy absorbed by a uniform material in a loading cycle (J $m^{-}3$)
d_1	Intrinsic dissipation heat source (J s^{-1} m^{-3})
$\tilde{d}_1$	Intrinsic dissipation source, average on a loading cycle (J s^{-1} m^{-3})
d_{1a}, d_{1b}	Intrinsic dissipation source above and below the fatigue limit (J s^{-1} m^{-3})
$\overline{E}$	Material Young modulus (MPa)
f_r	Cyclic loading frequency (Hz)
HCF	High cycle fatigue
PBF-LB/M	Laser Powder Bed Fusion, AM printing technology
m	Doudard's shape parameter
n	Lazan's damping exponent
$V_0 S_0$	Doudard's scale parameter[MPa^m mm3)
N_f	Number of cycles to failure
s_{the}	Thermoelastic heat source (J s^{-1} m^{-3})
SL	Step loading
CAL	Constant-amplitude loading
TCM	Two curves method
t	Time (s)
T_1	Loading cycle period during fatigue testing (s)
V_0	Microinclusion, microplasticization volume (mm^3)
ΔT	Mean surface temperature increment in a ROI
ΔT_s	Surface stabilization temperature in a ROI

can be considered as an indicator of the microstructural state of the material [3]. This state and its corresponding variation can be experimentally assessed [4] and compared with analytical predictions [5].

Hill, in [6], explains that in polycrystalline materials, at ambient temperature, the main damaging phenomenon is the slip mechanism, which leads to the formation of slip bands. In HCF on low-C steels, the slip bands start to be visible at $\frac{1}{100}N_f$. However, slip bands can form at dynamic loads that do not lead to fatigue failure. Another mechanism, which leads to fracture, is related to the dislocation movement. Under a cyclic load, the dislocation movement creates small deformations called 'extrusion' and 'intrusion'. These deformations are usually 10^{-3} mm, 10^{-4} mm in height and appear at $\frac{1}{10}N_f$ [6]. These defects usually grow, leading to cracking, which may lead to fracture or not. This phenomena is dominant for high stress levels.

Over the years, dissipative phenomena have also been analyzed by thermographic methods or self-heating measurements. In 1986 [7,8] characterize the heat dissipation distribution in dog bone specimens, comparing it to the electric resistance phenomena. The aim of these methods is to relate fatigue properties, such as fatigue limit, to the microstructure of the material [5,9]. Infrared thermography has been utilized in recent decades in a wide variety of applications involved in fatigue phenomena and fatigue limit determination, as deeply analyzed in [10–19].

In another study by Meneghetti et al. [20], presents a methodology to estimate the fatigue limit in 304L steel by thermal monitoring. Instead of using the temperature increment, the methodology of Meneghetti et al. [20,21] allows for the retrieval of heat dissipation from the cooling gradient. The main advantage of this method is that it does not require the specimen to be tested at the same frequency for each stress level in order to have comparable data. In subsequent studies by Meneghetti et al. [22] and Rigon et al. [23], the same methodology was applied on notched specimens and under multi-axial fatigue loading, respectively.

A probabilistic two-scale model was described in [24,25], which describes the microplasticization activation process and deduces both the corresponding intrinsic dissipation and the thermal increment of the specimen during fatigue testing. This model aims to provide a physical interpretation of the surface thermal increment considered as a fatigue damage parameter.

The Two Curves Method (TCM) [12] finds a difference in thermal emission's trend, and so in the intrinsic dissipation, in the case of a specimen tested above and below the fatigue limit. This suggests that the main damaging mechanism under the fatigue limit differs from the damaging mechanism when the stresses are higher. In particular, an evidence is found in the different slopes of the curves approximating the experimental data in the stress amplitude vs thermal increment plot.

Assuming that the damage can be related to microstructural modifications which can be directly linked to the intrinsic dissipation, the surface stabilization temperature of the TCM [12] is one of the most suitable to characterize the cumulated damage. Considering that the thermal emission of the specimen under cyclic loading is associated with local microplasticization phenomena and thermal hysteresis, it can be derived that thermal emission is proportional to the microstructural damage level. In additive manufactured materials the microstructural imperfection may have a stronger influence in the fatigue behavior, in fact pores are present, but also the presence of the weld pools might be assumed as a metallurgical imperfection and might influence the intrinsic dissipation.

Consider a scenario where it is necessary to explore various printing parameters through a Design of Experiments (DOE) testing campaign. A conventional staircase methodology would necessitate at least 15 specimens to determine the fatigue limit. If it becomes necessary to characterize different microstructures resulting from various printing parameters, the process could become prohibitively expensive, requiring the printing of hundreds of specimens for a fatigue characterization. However, if the characterization of the intrinsic dissipation yields accurate results in additive manufacturing (AM) materials, it could be possible to explore a multitude of printing parameters with a minimal number of tests per parameter. When discussing the dissipative aspects in additive manufactured materials, it is important to note that an additional layer of complexity is introduced in the modeling of these phenomena. In fact, the microstructure of additive manufactured materials presents numerous discontinuities, such as weld pools and laser tracks. In a study by [26], various methodologies were applied to study the fatigue behavior of additive manufactured materials. In particular, the temperature and the plastic strain amplitude, parameters that are also monitored in this work, were compared with the electric resistance of the tested specimen, which was used as a fatigue damage indicator. However, the study [26] focused on a low cycle fatigue range, where global plasticization is present. In a separate study [27], a passive thermography approach using step loading was presented to quickly estimate the fatigue limit. In this application, the focus was on additively manufactured 18Ni300 maraging steel and L40 tool steel, and the monitored parameter was the increase in surface temperature.

The present research primarily focuses on expanding our understanding of the dissipative aspects of materials produced through additive manufacturing processes. Then, the primary objective of this study is to establish a rapid and reliable evaluation method for estimating the fatigue limit of AM AISI 316L steel and, extending, for the AM alloys. A comprehensive exploration of these phenomena could potentially facilitate the application of rapid fatigue estimation methodologies to these materials. This would not only lead to a reduction in the duration of testing but also significantly decrease the expenses incurred during the material characterization phase. For instance, a step loading test could ideally require only a single test, and hence, a single specimen manufactured through additive processes.

The potential benefits of applying these methodologies to additive manufacturing processes are multiple. First, they could significantly reduce the time and cost associated with material characterization, particularly in the context of a DOE testing campaign. Secondly, they could enable for a more efficient exploration of various printing parameters, thereby facilitating the optimization of the manufacturing process. Lastly, by providing a more detailed understanding of the dissipative aspects in additive manufactured materials, these methodologies could contribute to the development of more reliable and durable AM products.

2. Analytical background

In this section, the analytical formulation of dissipative phenomena has been considered, referring to a flat specimen of indefinite length undergoing uniaxial loads. Based on the thermal equilibrium equation of a prism undergoing time-varying loading, the intrinsic dissipation will be modeled for two subcases, below and above the fatigue resistance stress amplitude.

This approach is based on the one-dimensional thermal diffusion equation described by Chrysochoos [5], simplified for a rectangular cross-section fatigued specimen of infinite length:

$$\rho c\dot{\theta} + \rho c\frac{\theta}{\tau_{eq}} = s_{the} + d_1, \tag{1}$$

where θ is the superficial thermal increment, c is the specific heat, ρ is the mass density, both assumed to be constant with respect to the internal state and thermodynamic state. s_{the} is the thermoelastic heat source, τ_{eq} is a time constant and d_1 is the intrinsic dissipation source. Thermal convection and radiation phenomena, and coupling between temperature and hardening variables are neglected, assuming an adiabatic phenomenon, as occurs, for example, in HCF tests. According to the literature, the modification of the sample surface temperature for Aluminum alloys ranges from 10 °C to 50 °C for steels [10] and therefore the change in temperature does not significantly affect the microstructural state, so the test condition of the material might be considered as at

ambient temperature. The mean heat sources in each cross section are representative of the overall thermal behavior of the cross section, and the heat source distribution is constant throughout the specimen gauge. Since the total thermo-elastic power is null in a fatigue cycle, only the intrinsic dissipation d_1 needs to be considered in the thermo-mechanical equilibrium:

$$\dot{\tilde{\theta}} = \frac{\tilde{\theta}}{\tau_{eq}} = \frac{\tilde{d_1}}{\rho c}, \tag{2}$$

where $\tilde{\theta}$ is the mean superficial thermal increment. By integrating Eq. (2), the *mean temperature* in a fatigue cycle can be calculated as follows:

$$\tilde{\theta} = \frac{\tau_{eq}}{\rho c}\left[1 - \exp\left(-\frac{t}{\tau_{eq}}\right)\right]\tilde{d_1}, \tag{3}$$

In case of periodical loading, the final expression of surface thermal increment depends on the adopted mathematical model for intrinsic dissipation d_1 and may be related to different damage mechanisms, respectively below and above the fatigue limit, following the classical Feltner's hypothesis.

2.1. Below fatigue limit

In the stress range below the fatigue limit, involving mainly anelastic phenomena, according to Giovannozzi [28], following the classical Föppl's approach, the applied stress $\sigma(t)$ may be written as $\sigma(t) = \Sigma_0 \sin(\omega_r t)$, where ω_r is the loading pulsation and the corresponding strain $\epsilon(t)$ as $\epsilon(t) = \Omega_0 \sin(\omega t + \varphi)$, where Σ_0 is the stress amplitude, Ω_0 is the strain amplitude, φ is the phase angle related to structural damping, which causes a delay between stress and strain. Dissipated energy in this stress field can be assessed as the area of the hysteresis cycle in the strain–stress experimental plot in uniaxial testing, having an elliptical form. According to Lazan [29], the related so-called damping energy D, unit energy absorbed by a macroscopically uniform material volume in a loading cycle can be expressed by the following formula:

$$D = \zeta \Sigma_0^2, \tag{4}$$

where ζ is the damping constant, and the numerical value 2 corresponds to the damping exponent for linear anaelastic damping and low stresses [29]. The hysteresis loop area A_h, depending only on the macroscopic alternate stress component Σ_0 can be calculated as follows:

$$A_h = \int_0^{2\pi} \Sigma_0 d\epsilon = \Sigma_0 \Omega_0 \sin\varphi\pi, \tag{5}$$

For typically small values of structural damping [29], as in the case of metallic materials, $sin\varphi$ can be approximated with the corresponding phase angle φ, also known as *loss angle*. For a linear homogeneous material with Young's modulus $\overline{E}$, assuming a small area approximation, the following approximation may be adopted:

$$\Sigma_0 \cong \overline{E}\Omega_0, \tag{6}$$

so that

$$A_h \cong \overline{E}\Omega_0^2 \sin\varphi\pi \cong \frac{\Sigma_0^2}{\overline{E}} \sin\varphi\pi. \tag{7}$$

To express the dissipated power in time unit, the hysteresis cycle area is multiplied by the test frequency $f_r = \omega_r/2\pi$. The intrinsic dissipation $\tilde{d_1 b}$ over a cycle of period T_1, for loading condition below the fatigue limit, can be obtained as:

$$\tilde{d_{1b}} = \frac{1}{T_1}\int_t^{t+T_1} d_{1b} dt = f_r \int_t^{t+T_1} d_{1b} dt = f_r A_h \cong f_r \frac{\Sigma_0^2}{\overline{E}} \sin\varphi\pi. \tag{8}$$

According to Eqs. (7) and (8), the dissipated energy is proportional to the square value of the alternate stress component. Substituting Eq. (8) into Eq. (3), the mean surface temperature increment can be obtained as follows:

$$\tilde{\theta} = \frac{\tau_{eq}}{\rho c}\left[1 - e^{\left(-\frac{t}{\tau_{eq}}\right)}\right]\tilde{d_{1b}} \tag{9a}$$

$$\tilde{\theta} = \frac{\tau_{eq}}{\rho c}\left[1 - exp\left(-\frac{t}{\tau_{eq}}\right)\right]\frac{sin\varphi\pi f_r}{\overline{E}}\Sigma_0^2. \tag{9b}$$

Eqs. (3) and (9b) are represented by an exponential law relating the *mean superficial thermal increment* in a fatigue cycle to the corresponding dissipated power in a time unit and, as a consequence, relating the mean temperature to the hysteresis area.

2.2. Above fatigue limit

In the stress range above the fatigue limit, a law describing the micro plasticization activation in a metallic material subjected to HCF has been adopted, treating micro-plasticizations as micro-inclusions in the elastic matrix of the material, similar to the theory of Eshelby [10]. In this work, only the basic version of the above-mentioned approach, referring to uniaxial loads, has been considered.

Table 1
Applied laser parameters for the manufacturing of the specimens.

Parameter	Core	Downskin
Energy density E [J/mm^3]	65.00	22.86
Laser power P [W]	192.00	80.00
Scan velocity μ [mm/s]	750.00	2500.00
Hatch distance h [mm]	0.1	0.035
Layer thickness t [mm]	0.04	0.04

In particular, a probabilistic two-scale model describing the micro-plasticization activation process has been taken into account and the corresponding intrinsic dissipation and specimen thermal increment were deduced. In this model the Poisson Point Process of intensity λ is defined, on the basis of two parameters Weibull model. So, λ may be calculated from the following relation:

$$\lambda(\Sigma_0) = \frac{1}{V_0}\left(\frac{\Sigma_0}{S_0}\right)^m. \tag{10}$$

By developing the free energy associated with an elastoplastic inclusion, it is possible to evaluate the global dissipated energy density $\Delta(\Sigma_0)$ due to microplasticization activation in a cycle:

$$\Delta\left(\Sigma_0\right) = \frac{4m}{h(m+1)(n+2)}\frac{\Sigma_0^{m+2}}{S_0^m}, \tag{11}$$

where V_0 is the microinclusion/microplasticization site volume, m and S_0^m are the model shape and scale parameters, respectively (dependent on the material). Similar to Eq. (9b), the mean value of intrinsic dissipation d_{1a} per cycle above the fatigue limit can be calculated as follows:

$$\tilde{d_{1a}} = f_r\Delta\left(\Sigma_0\right) = f_r\frac{4m}{h(m+1)(m+2)}\frac{\Sigma_0^{m+2}}{S_0^m}. \tag{12}$$

From Eq. (12), the relationship between the steady-state or stabilization temperature and the alternate stress component Σ_0 is found. By integrating Eq. (2), the following expression for the general temperature increase is obtained:

$$\tilde{\theta} = \frac{m\eta V_0}{(m+1)(m+2)V_0S_0^m}\left[1-\exp\left(-\frac{t}{\tau_{eq}}\right)\right]\Sigma_0^{m+2}, \tag{13}$$

where ηV_0 represents the term describing the kinetics of the thermal phenomena for an inclusion volume V_0:

$$\eta V_0 = \frac{4f_r\tau_{eq}}{h\rho c}V_0, \tag{14}$$

where h corresponds to the hardening modulus. For stresses above the fatigue limit, involving micro-plasticity activation and dislocation motion, the intrinsic dissipation may be expressed by the corresponding thermal emission and the related increment of the thermal profile in the stabilization zone (steady-state temperature). The corresponding thermal increment depends on the alternate stress component: in the case of Eq. (12), the thermal increment does not depend on the square of the alternate stress component but on the power $(m+2)$, which is usually higher than 2. From a mechanical point of view, the damping energy expression D (Eq. (4)) shows an exponent n usually larger than 2, and the corresponding hysteresis cycles are nonlinear and not elliptical. Similar considerations can be made by analyzing the problem in a dynamic framework. The loss angle defined in Eq. (5), for small values of structural damping, is related to the loss coefficient h in a complex notation. In particular, referring to an energy approach, the dimensionless loss coefficient h is defined by Lazan [29] as the ratio of damping energy to strain energy, and this coefficient increases with the number of cycles in HCF tests above the fatigue limit in mild steels.

3. Material

In this investigation, 316L stainless steel (1.4404) metal powder, supplied by Oerlikon Metco, was utilized to prepare the specimens by means of the Laser Powder Bed Fusion (PBF-LB/M) technology. An EOS M280 PBF-LB/M machine was used, equipped with a 400 W Ytterbium continuous wave fiber laser. The metal powder possessed particle sizes ranging from 20 to 63 μm, with respective volume percentile values of D10, D50, and D90 measuring 19 μm, 30 μm, and 46 μm. During the manufacturing process, Argon 5.0 gas was employed, and efforts were made to maintain a residual oxygen concentration below 1300 ppm within the build chamber. The printing parameters are detailed in Table 1.

Notably, the specimens were not subjected to post-processing. This as-built condition ensures a microstructure that is finer than the annealed one, thereby enhancing the fatigue limit [30–33]. The surface retained the as-built roughness to closely mimic the operating conditions of additive manufactured components. Roughness measurements are reported in Section 5.1. Two sets of specimens were manufactured, round and flat. The hardness of the material ranges between 215 to 230 HV1. The geometry of the samples used in this investigation is reported in Fig. 1 and was designed according to the guidelines specified in ASTM E466 [34].

To mitigate the stress concentration in the edge region of the flat specimen [35], a fillet with a radius of 1 mm was introduced along the four edges.

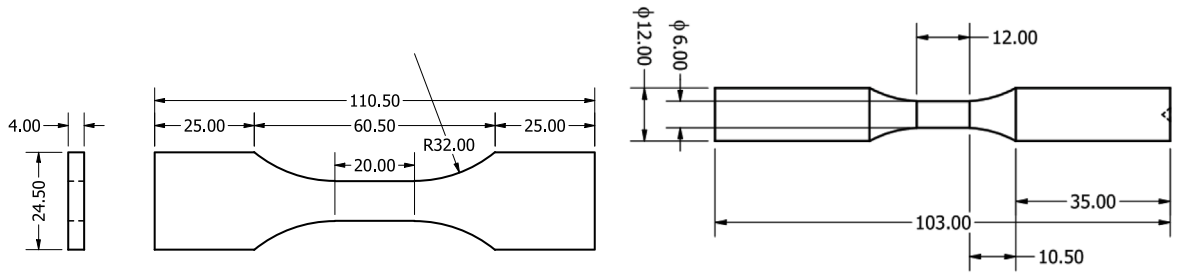

(a) flat specimen (b) round specimen

Fig. 1. Fatigue and tensile specimens geometry according to ASTM E466 [34], dimensions in mm.

4. Methodology

In this section, all the methodological aspects of the tests will be presented.

4.1. Surface roughness measurement

The Keyence VK-1000 laser confocal microscope was employed for assessing the surface roughness, line roughness, and surface topology. The measuring line was, in the central specimen area, parallel to load direction. The measurement of line roughness utilized a cutoff wavelength (λ_c) of 0.25 mm and an evaluation length (λ_s) of 25 μm.

4.2. Microstructure

The porosity measurement was conducted using a GE Phoenix Nanotom S μ-computed tomography machine, operating at a voltage of 180 kV. To mitigate the beam hardening effect, a copper filter with a thickness of 0.5 mm was employed. The acquisition parameters included 1440 projections, with an angular increment of 0.25° per image and an exposure time of 1500 ms. With this configuration, a voxel resolution of 3.749 μm/voxel was achieved.

4.3. Mechanical testing

Monotonic and fatigue tests were performed utilizing an *Instron 8800* test frame, integrated with an *Instron 8500 digital* control system (Instron mechanical testing systems, USA). This system boasts a dynamic load capacity of ±100 kN. Tensile tests on 3 flat specimens have been performed in order to assess the quasi-static properties of the material.

The primary objective of this study is to study the applicability of a rapid evaluation method for estimating the fatigue limit in additive manufactured steel specimens based on the analysis of both mechanical and thermal parameters acquired during testing. In this context, according to literature for bulk steel specimens, step-loading (SL) tests are indicated as the most suitable as they allow for the exploration of the entire stress range of the cyclic load, both below and above the fatigue limit, of intrinsic dissipation and self-heating of the specimen across the entire stress level range within a single test. Ideally, this could facilitate the evaluation of the material's fatigue limit within just one test. However, a single SL test is insufficient for a reliable characterization of the dissipative phenomena. Therefore, much of the research in the technical literature explores the intrinsic dissipation across different stress levels using constant amplitude loading (CAL) tests.

To achieve this, the fatigue test campaign was then designed to examine the dissipative and thermal aspects during SL and CAL tests for 1 million of cycles. In the CAL testing campaign, 12 flat specimens have been tested. Each CAL test was conducted for flat specimens for each stress level, in push-pull configuration $R = \frac{\sigma_{min}}{\sigma_{max}} = -1$, starting from σ_a = 80 MPa and increasing to 300 MPa with a stress increment of 20 MPa between each level. The test frequency has been set to 15 Hz. In an effort to further validate the robustness and reliability of the adopted methodology, special attention was given to the potential influence of variations in specimen geometry and stress ratio. Then the first SL testing campaign was run on flat specimens with $R = -1$ at different testing frequencies (10, 15, 30 and 45 Hz), one specimen per frequency. Results obtained at 10 Hz did not give a reliable surface temperature increment; at 15 Hz the best trade off between temperature increment and strain measurement quality was found; at 30 Hz the trade off was not optimal and at 45 Hz the surface temperature increment was maximized and the strain measurements were not reliable. This paper will then present the SL and CAL tests performed at 15 Hz, and additionally for SL at 45 Hz.

A second test set was run on two cylindrical specimens, with $R = 0.1$, 15 Hz, using the SL testing methodology, to prove the methodology also for a different geometry and with a different stress ratio. This batch of specimens has been previously tested in an earlier study, and their fatigue behavior was well-documented and discussed in [36] .

Throughout each test, the strain was measured using a strain gauge for the entire duration. Similarly, the temperature was recorded using a PI-400 IR camera. The specimens were black painted to assess emissivity, which was then set to 0.95. Additionally,

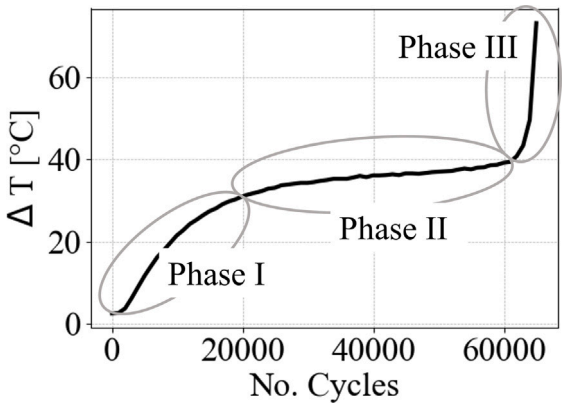

Fig. 2. Typical surface temperature vs cycle trend in fatigue testing of a metallic specimen.

a reference specimen was attached to the lower grip of the testing machine to provide a reference temperature value (see Fig. 3). This is because the temperature of the lower grip of the hydraulic testing machine varies during tests down due to the oil mass flow, which is subject to heating or cooling due to the chiller cooling action.

4.3.1. Murakami method estimation

Murakami's method [37], provides a framework for predicting the influence of surface roughness on fatigue life by means of a dedicated parameter quantifying the actual influence of the roughness dimension and shape, the $\sqrt{Area}$ parameter. This parameter is especially significant when considering the spatial distribution of roughness peaks. The corrected formulation, which incorporates a factor of $2b$ (representing the spatial distribution of roughness peaks), is given by:

$$\frac{\sqrt{Area_R}}{2b} \approx 2.97\left(\frac{a_M}{2b}\right) - 3.51\left(\frac{a_M}{2b}\right)^2 - 9.74\left(\frac{a_M}{2b}\right)^3, \tag{15}$$

where this relation holds for $\left(\frac{a_M}{2b}\right) < 0.195$. For values of $\left(\frac{a_M}{2b}\right) > 0.195$, the relationship simplifies to:

$$\frac{\sqrt{Area_R}}{2b} \approx 0.38. \tag{16}$$

In [37], it is recommended to use the highest measured peak, denoted as Rt, as the defect depth (a_M). For the periodic defect distribution parameter ($2b$), the roughness parameter Rsm is considered the most appropriate due to its close alignment with the definition. In [38] he further deepens the nature of scatter in fatigue life.

A more recent study in [39] delves into the effects of high surface roughness, especially in as-built additive manufactured materials. While traditional materials or polished specimens predominantly exhibit short crack modeling for fatigue behavior description, as-built rough AM materials present a more complex scenario. Such materials exhibit a behavior that is a hybrid of short and long crack propagation modes. This mixed behavior becomes particularly pronounced for $\sqrt{Area}$ values exceeding 1000 μm. In the context of our study, the critical scenario arises when $a_M/2b > 0.195$. Under these conditions, the predicted fatigue limit is expected to be at its lowest, indicating a heightened vulnerability to fatigue. Therefore the fatigue limit is calculated as:

$$\sigma_d = 1.43 * \frac{HV + 120}{\sqrt{Area_R}^{1/6}} * \left(\frac{1-R}{2}\right)^{0.226+(HV*10^{-4})} \tag{17}$$

4.3.2. TCM iterative method for fatigue limit estimation

In this section, the methodology used for the fatigue limit estimation basing on passive thermography parameters, acquired during fatigue testing, is presented. As described in [10], when a specimen undergoes HCF testing, the surface temperature shows three typical trends (Fig. 2): an initial non linear increment (phase I) which generally lasts within 5000 loading cycles, a linear trend (phase II) and, when crack propagates, a non linear increment until failure (phase III). As regards phase II, the trend can be horizontal (stabilized on a so called stabilization temperature) or with both positive or negative linear slope. So further considerations are needed. In [40], the second phase related phenomena are described. To define a unique thermal parameter to describe the dissipating behavior in phase II, in [10], a parameter is defined by considering the thermal increment at a given number of cycles in phase II, in particular, the temperature increment after 15 000 cycles for the CAL test and at the end of the step for the SL test. This parameter will be generally hereafter called *stabilization temperature* $\overline{\theta}$.

Stabilization temperature $\overline{\theta}$ in phase II, is a reliable parameter to monitor when using this thermographic technique [10]. Other parameters defined in [10] will be applied in the present paper. The *mean surface temperature increment* ΔT is the increment of surface temperature with respect to ambient, averaged over a ROI, during testing. This parameter follow the trend of surface temperature and then a stabilized value corresponding to phase II ΔT_s can be defined.

In the present research, the thermal parameter $\overline{\theta}$ is experimentally estimated through ΔT_s with test with stress amplitude ranging from very low values to close the yield stress, then above and below the fatigue limit, in order to analytically evaluate the limit. In the case of a cyclic loading below the fatigue limit, Eq. (9b) simplifies to:

$$\overline{\theta} = \frac{\tau_{eq}}{\rho c} \frac{sen\varphi \pi f_r}{\overline{E}} \Sigma_0^2. \tag{18}$$

In case of loading amplitude above the fatigue limit, Eq. (13) reduces to:

$$\overline{\theta} = \frac{4 f_r \tau_{eq} m}{h \rho c (m+1)(m+2)} \frac{\Sigma_0^{m+2}}{S_0^m} \tag{19}$$

The methodology to estimate the fatigue limit employed in this study is based on the Two Curves Modified Iterative Method as described in [12].

4.4. Iterative algorithm

The determination of the fatigue limit is achieved through an iterative process which considers both the data trend and potential inaccuracies in the curve fitting. The process is detailed as follows:

To begin the iterative process, a search space for the prospective fatigue limit is defined. This space is essentially a range of possible values that the fatigue limit could assume, based on the initial understanding or estimations.

In each iteration, the dataset is divided into two subsets based on the current guess for the fatigue limit and the defined exclusion radius:

Below the Fatigue Limit: This subset, denoted as D_{below}, comprises data points that are within the exclusion radius below the current fatigue limit guess. Mathematically, if F is the current fatigue limit guess and R is the exclusion radius, then:

$$D_{\text{below}} = \{x | x < F - R\}$$

Above the Fatigue Limit: This subset, denoted as D_{above}, contains data points that are outside the exclusion radius above the current fatigue limit guess:

$$D_{\text{above}} = \{x | x > F + R\}$$

According to technical literature, as for example [41], or standards (UNI3964), the variability of experimental results on the so-called 'fatigue limit' is usually about 10 to 20 MPa. In the present work, the exclusion radius has been chosen as $R = 15$MPa.

For each subset (above and below the fatigue limit), a curve is fitted to the data:

- Let $f_{\text{below}}(x)$ be the curve fitted to D_{below}.
- Let $f_{\text{above}}(x)$ be the curve fitted to D_{above}.

It is essential to ensure C^0 continuity, implying that the two curves intersect it the fatigue limit without any discontinuity:

$$f_{\text{below}}(F) = f_{\text{above}}(F)$$

Four different equations have been used to model the curve, the presented parameter a, b, d, e, l, m, p, q are fitting parameter that are given as output by the fitting algorithm as it finds the best fitting curve. As regards the part of the curve below the fatigue limit has been defined a parabola through the origin, that has been introduced in [10]:

$$f_1(x) = a \cdot x^2. \tag{20}$$

For simplicity, a line through the origin is also used to model the behavior below the fatigue limit:

$$f_2(x) = m \cdot x. \tag{21}$$

As regards the part of the curve above the fatigue limit, it is possible again to fit the data along a line, but a modification is needed to ensure the C^0 continuity in F. So, for the line, the equation becomes:

$$f_3(x) = m \cdot (x - l) + d, \tag{22}$$

where $l = F$ and $d = f_{\text{below}}(F)$.

Similarly a power law can be defined by the following equation:

$$f_4(x) = a \cdot (x - p)^b + e - a \cdot (q - c)^b. \tag{23}$$

The equation has been modified to assure the continuity, and in particular $q = F$ and $e = f_{\text{below}}(F)$.

The error, E, is determined based on the residuals from the curve fitting process for both subsets. It quantifies the difference between the actual data points and the values predicted by the fitted curves. We exclude from the error calculation the experimental values using the exclusion radius as shown in Section 4.4. We define y_{exp} as the experimental measurements corresponding to the sample of the dataset D and used in the fit:

$$E_{below} = \sum \left(y_{exp,below} - f(D_{\text{below}})\right)^2 \tag{24}$$

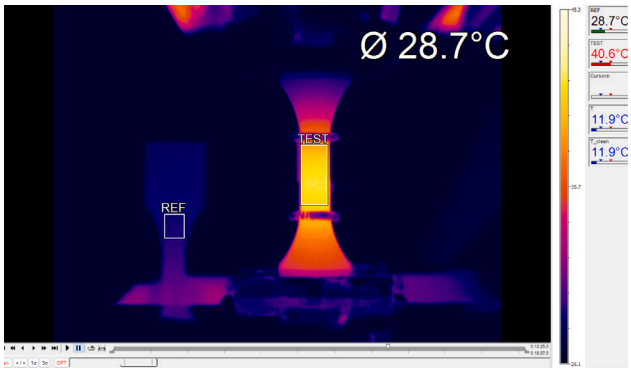

Fig. 3. Passive thermography typical acquisition frame: tested specimen surface temperature contour (TEST) and reference temperature contour (REF).

$$E_{above} = \sum \left(y_{exp,above} - f(D_{\text{above}})\right)^2 \tag{25}$$

$$E = E_{below} + E_{above} \tag{26}$$

The objective of the iteration is to minimize this error. The fatigue limit, F, and the curves f_{below} and f_{above} that produce the smallest error are stored.

Algorithm 1 Iterative determination of fatigue limit

Require: Dataset, Exclusion radius, Initial Search Space for F
  Initialize error as infinity
  for each F in the Search Space **do**
    Partition dataset into D_{below} and D_{above}
    Fit curves f_{below} and f_{above} ▷ The C^0 continuity is assured by the equation definition
    Compute error, E
    if E is smaller than previous iterations **then**
      Store F, f_{below}, and f_{above}
    end if
  end for
    return Optimal F, f_{below}, and f_{above}

The iteration ensures the most accurate determination of the fatigue limit, providing a robust foundation for subsequent analyses.

5. Results and discussion

In this section, we present the results of the experimental campaign and we discuss the thermal behavior and mechanical dissipation of the tested specimens.

5.1. Surface roughness

The surface roughness of the specimens was measured and the results are presented in Table 2. The mean values and standard errors for the roughness parameters R_a, R_z, S_a, R_{sm} and S_z are reported. The surface topology of the 316L specimens, fabricated using the PBF-LB/M method, is reported in Fig. 4. The image distinctly shows the presence of partially melted metal particles on the surface. These particles, due to their irregular shape and size, can induce high stress concentrations, which potentially reduce the fatigue life of the material. This evidences and their effect on fatigue behavior will be further discussed in 5.4.

5.2. Density

The density of the specimens was evaluated using micro-computed tomography (μ-CT) measurements. The results revealed an impressive density of 99.996%, indicating high material compactness. In addition to density, the sphericity of the observed pores was also measured, with an average value of 0.68. Sphericity is a critical parameter as higher sphericity reduces stress concentration at the pores, thereby decreasing the likelihood of crack initiation at internal defects. This aspect is particularly important in fatigue studies, where internal defects can significantly influence the fatigue life of a material.

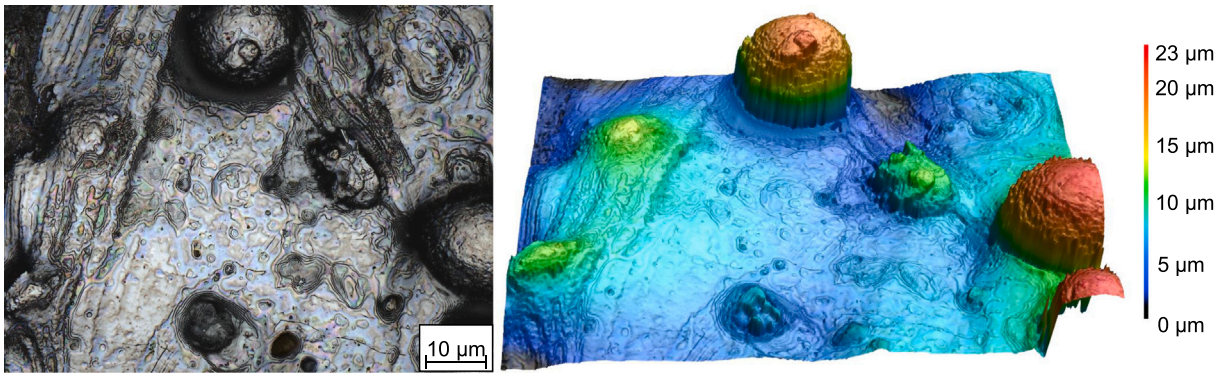

Fig. 4. Surface Topology of PBF-LB/M Manufactured 316L Specimens, highlighting the presence of partly melted metal particles on the surface.

Table 2
Results of surface roughness measurements.

	R_a [µm]	R_z [µm]	S_a [µm]	S_z [µm]	R_{sm} [µm]
Mean value	8.15	47.28	8.77	107.74	135.37
Standard deviation	1.77	6.91	1.54	42.25	9.51

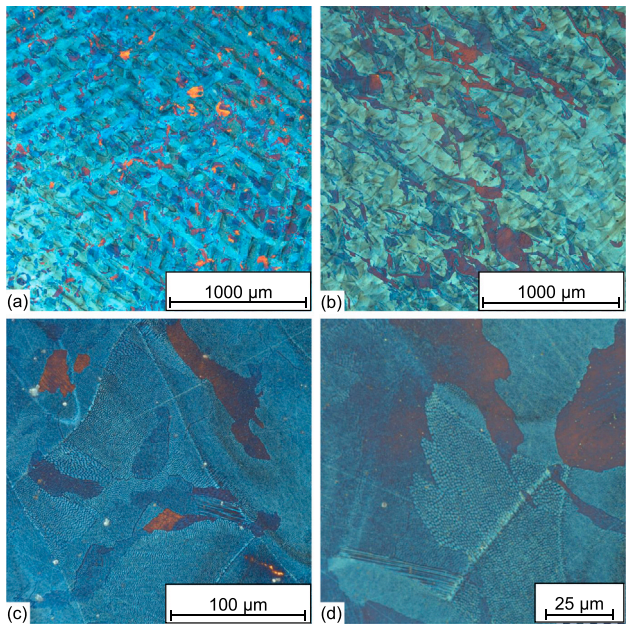

Fig. 5. Microstructure analysis of 316L manufactured via PBF-LB/M process; (a) cross-sectional view (b) transversal view (c) distinct grain boundaries represented by various colors, (d) fine subgrains, 300–400 nm width, within the larger grains.

5.3. Microstructure

The microstructure of the 316L specimens is illustrated in Fig. 5. Figs. 5(a) and (b) depict the melt pool geometry from cross-sectional and transversal perspectives, respectively. These images provide an understanding of the solidification process and the resulting microstructural features. A closer examination of the microstructure, as shown in Figs. 5(b) and (c), reveals the presence of fine cellular subgrains. These subgrains are a direct result of the rapid cooling rate inherent to the PBF-LB/M process. The formation of these subgrains contributes to an increase in yield strength while maintaining a high elongation at fracture [42]. This phenomenon, known as grain boundary strengthening, is a well-documented effect and can be described by the Hall-Petch relationship [43]. The microstructural analysis thus provides valuable insights into the material mechanical properties and its potential performance under fatigue loading.

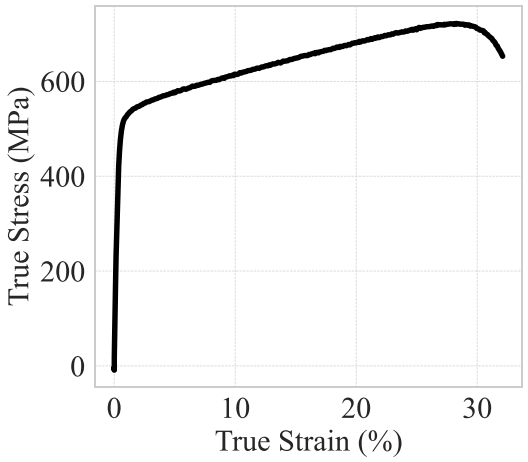

Fig. 6. Tensile test curve.

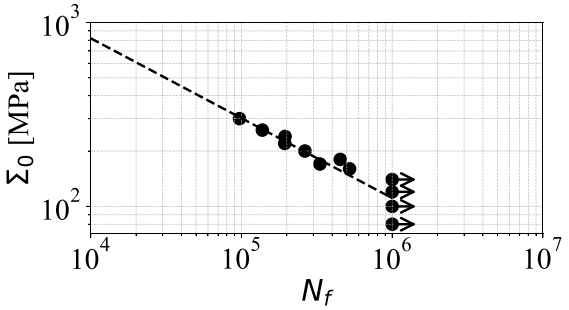

Fig. 7. S-N diagram of CAL testing campaign (flat specimens).

5.4. Mechanical testing

The results of the tensile test for one specimens are reported in Fig. 6 as an example. The yielding point of this specific material, when printed with the given parameters and manufactured into a flat specimen, is approximately 520 MPa. In [36] the results related to cylindrical specimens are reported and the yield stress is 471 MPa. Furthermore, in both configurations, the material exhibits a remarkable elongation to rupture, exceeding 30%. This suggests that the material not only possesses high strength but also demonstrates significant ductility.

Regarding the fatigue testing campaign, the experimental data related to flat specimens are plotted on a log–log scale S-N plot in Fig. 7.

As can be observed, the material, in flat specimens, presents a fatigue resistance (1 million cycles) about 150 MPa, more than 3 times lower than the yield stress. This value was estimated as the maximum stress amplitude where no failures were recorded at 1 million cycles. For bulk flawless steels, according to a popular thumb rule [37], the *ideal fatigue limit* of a material $\sigma_{D-1} = 1.6 * HV$, neglecting roughness and pores weakening effects. Furthermore experimental evidence from technical literature [44] reports a fatigue limit of 150 MPa for wrought material. In the present case, the hardness ranges between 215-230HV (see Section 3) and it leads to an *ideal fatigue limit* of 344 MPa. The AM material shows a strongly weakened behavior. The large difference between the experimental fatigue limit and the material ideal fatigue limit is relatable to the high surface roughness and porosities that strongly weaken the material with respect to resistance to cyclic loading.

Round specimens have been tested in order to build their S-N curve with $R = 0.1$, showing a fatigue limit $\sigma_{0,1}$ of about 100 MPa. Even if the geometry of the specimen was different, the flat specimen did not show any corner nucleated crack, due to the corner fillet as suggested in [35].

The fatigue limit has also been estimated by means of the Murakami method, with respect to different roughness parameters and loading ratio R. The result are hence presented in Table 3.

It results that the Murakami method, used with the selected roughness parameters, does not properly predict the experimental fatigue resistance of AM material. The reason might be explained by [45]. In fact, for AM materials, the surface has irregularities due to stuck powder grains on the surface. Standard roughness testing, laser profilometry, or any other technique which can measure from superficial exploration, can miss the complexities in the profile, hidden in the surface. In [45] a comprehensive study is presented, and it is shown how this can strongly affect the estimation.

Table 3
Murakami prediction of infinite fatigue resistance.

Roughness parameter	R_a	R_z	S_a	S_z
Murakami prediction (R=−1)	286 MPa	249 MPa	283 MPa	249 MPa
Murakami prediction (R=0.1)	235 MPa	204 MPa	232 MPa	204 MPa

Table 4
Fatigue resistance estimations and total error in curve fitting according to different fitting curves. σ_D [MPa] stands for σ_{D-1} for $R = -1$ tests and $\sigma_{D0.1}$ for $R = 0.1$ tests.

Model	$\sigma_{D,parabola-power}$	$error_{parabola-power}$	$\sigma_{D,line-power}$	$error_{line-power}$	$\sigma_{D,line-line}$	$error_{line-line}$
CAL_{temp}	165	3.5e+00	165	3.2e+00	205	1.7e+00
CAL_{hys}	155	1.8e−04	145	2.6e−04	175	4.8e−04
$SL_{f=15Hz,flat,R=-1,hysteresis}$	129	0.0	129	1.0e−06	165	8.9e−06
$SL_{f=15Hz,flat,R=-1,temperature}$	139	1.6e−01	136	1.2e−01	179	8.0e−01
$SL_{f=45Hz,flat,R=-1,temperature}$	111	3.4e−02	108	4.4e−02	131	2.9e−01
$SL_{f=15Hz,round-1,R=-1,temperature}$	142	9.4e−02	140	1.4e−01	144	1.5e−01
$SL_{f=15Hz,round-2,R=-1,temperature}$	114	5.7e−02	105	8.7e−02	96	2.2e−01
$SL_{f=15Hz,round-2,R=-1,hysteresis}$	115	1.0e−06	115	1.0e−06	121	0.0

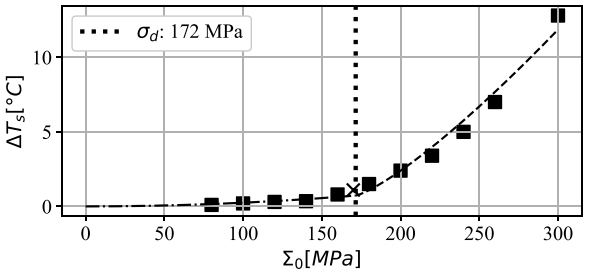

Fig. 8. TCM-modified applied to CAL ΔT_s data, R = −1.

Hence, the fatigue limit has been estimated as presented in Section 4.4, using all the discussed curves. A complete presentation of the results is presented in Appendix Table 4. In the following section, for sake of brevity, only the main insight will be reported.

5.4.1. Thermographic approach for CAL tests

From here below the results presented in the figure follows this standard: the experimental data used in the fitting of the optimal fatigue limit are plotted as (square), while the one excluded are plotted as (x). Then the optimal fatigue limit resulted from the iterative algorithm is presented as a vertical dotted line (..), the curve fitted below the fatigue limit is presented as (-.) and the curve fitted above is presented as (–). Hence in the legend the numerical value of the optimal fatigue resistance is reported.

The first set of results of thermographic analyses of fatigue tests is related to the CAL series. As shown in Fig. 8, the stabilized temperature increment ΔT_s vs stress amplitude shows a trend similar to that observed in bulk materials. This alignment is a testament to the consistency of the material response to HCF loading, as reported in technical literature [10–12].

For the hysteresis cycle area, as shown in Fig. 9, the trend of data for stress amplitude below the fatigue resistance clearly adheres to a bi-power law. This relation is a well-established mathematical model used to describe the behavior of materials undergoing elastic cyclic loading. However, the same consistency is not observed for the stabilization temperature (Fig. 8). This discrepancy is likely due to the 15 Hz testing frequency, which fails to sufficiently increase the surface temperature of the flat specimen, due to low dissipated energy in time unit and conduction phenomena through grips which affect the adiabaticity hypothesis. This limitation is a critical aspect of fatigue testing, as the temperature increment is directly linked to the energy dissipated in the time unit and in thermal equilibrium conditions.

In this context, the anelastic component of intrinsic dissipation, related to the microplasticization site activation, is minimal at 15 Hz. This leads to inefficiencies in the iterative algorithm, which is designed to predict the material response basing on the dissipated energy. Nevertheless, it can be noted that the fatigue resistance stress is attained at this testing frequency, albeit with a noticeable temperature increase, as depicted in Fig. 8.

5.4.2. Thermographic approach for SL tests

While the CAL testing was primarily performed to characterize the dissipative and thermal properties of the material, its secondary objective was to validate the thermal dissipation models. One of the most significant benefits of this testing methodology is its ability to rapidly estimate the fatigue limit. According to literature for bulk steel, once the model is validated, then SL test allow for a faster and cheaper assessment of fatigue limit. The same procedure is here applied to AM specimens and the results of SL tests are here presented.

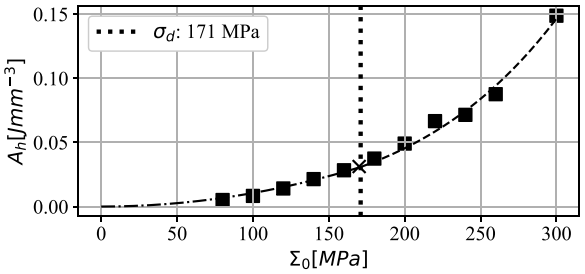

Fig. 9. TCM-modified applied to CAL Hysteresis area data, R = −1.

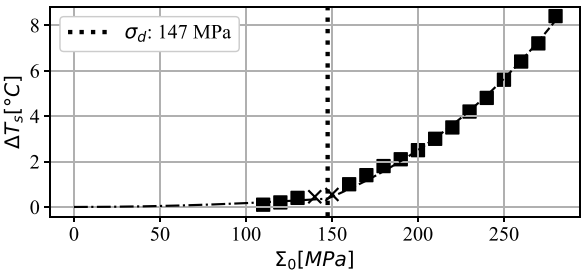

Fig. 10. TCM-modified applied to SL ΔT_s data, 15 Hz, R = −1.

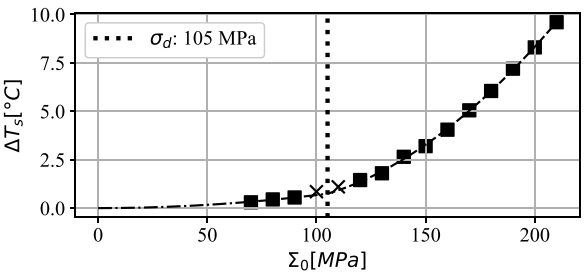

Fig. 11. TCM-modified applied to SL ΔT_s data, 45 Hz, R = −1.

Employing a load ratio of $R = -1$, the testing frequency was varied. This variation aimed to optimize thermal dissipation, highlighting the inflection point, or 'knee', in the curve representing stabilized surface thermal increment ΔT_s versus alternate stress. One challenge in CAL testing was the minimal temperature increment observed for stress levels below the fatigue resistance. To address this, an additional test was conducted at 45 Hz frequency.

As depicted in Fig. 10, a noticeable change in the data trend is evident around 150 MPa. Above this stress level, the curve follows a power-law trend, indicating behavior beyond the fatigue limit. Conversely, for stress levels below 150 MPa, the curve remains relatively flat, with negligible temperature increments. Regarding the SL test at 45 Hz, even though fewer steps were executed, the temperature increments were more pronounced (Fig. 11). This distinct behavior facilitates the clear identification of the bi-power law trend when operating below the fatigue resistance.

Fig. 12 illustrates the differences in the hysteresis cycle for two distinct loading stress amplitudes. Notably, even though both scenarios operate within the elastic range, there is a pronounced difference in the area of the hysteresis cycle. This data point out the significance of anelasticity and microplasticization phenomena in influencing the material dynamic and dissipative behaviors.

5.4.3. Thermographic approach for SL tests on round specimens

Fig. 13(a) shows the results from one of SL tests on round specimens as an example. An evident knee in the curve can be readily identified around 100 MPa. However, it is important to highlight that the test results exhibited considerable variability, especially in the stress range between 80 MPa and 120 MPa.

In Fig. 14(a) the evolution of hysteresis loop area during a SL test is presented. The results, accordingly to [46], can be explained by micro-structure changes leading to material hardening. However, the model, described in Eq. (1), considers a distributed dissipation due to a distributed heat source. Nevertheless, in the last phase of the test the crack is probably already nucleated, and then localized plastic phenomena, well described in [46] generate heat increments which stabilize during the single step. Similarly in [40] the similar behavior is found in the surface temperature increase, explainable as an hardening of the material.

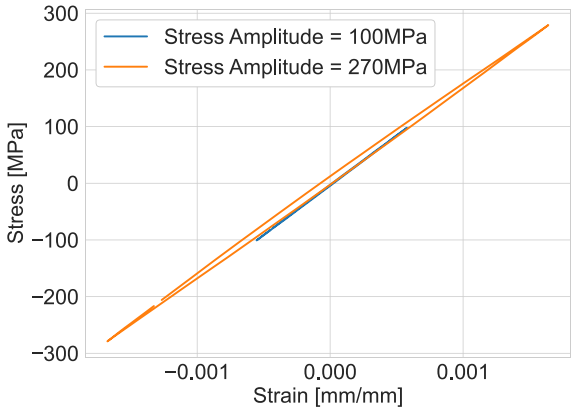

Fig. 12. SL-15 Hz-R=-1 - Comparison of Hysteresis Cycles for Different Stress Amplitudes.

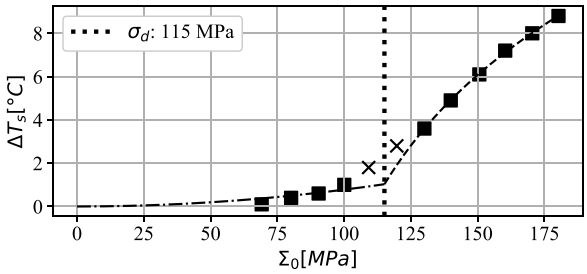

(a) ΔT_s data per each loading step

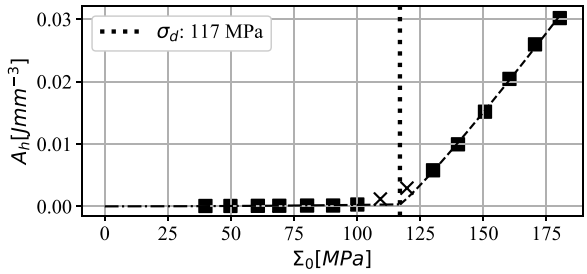

(b) Hysteresis cycle area per each loading step

Fig. 13. TCM-modified - SL test, Round specimen, testing frequency 15 Hz, R = 0.1.

One of the most salient insights derived from these tests is the methodology's capability to account for the influence of stress ratio on fatigue behavior.

6. Conclusion

This study has provided a comprehensive exploration of the fatigue behavior of 316L stainless steel specimens, focusing on those produced using the PBF-LB/M method. The results from the experimental campaign provide insightful information about the fatigue behavior of 316L stainless steel specimens produced using the PBF-LB/M method and about the feasability of thermographic technique for fatigue limit assessment. Several key observations can be drawn:

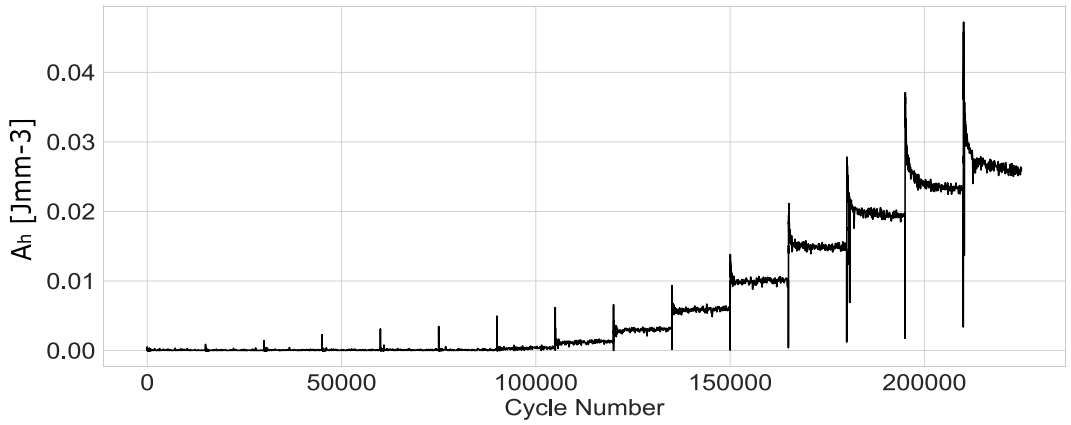

(a)

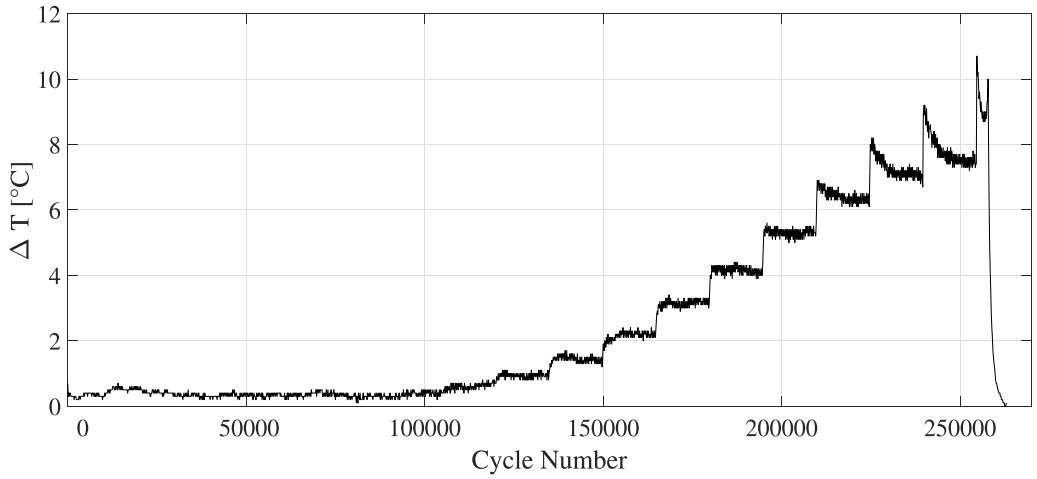

(b)

Fig. 14. Intrinsic dissipation (a) and Average surface temperature increase (b) vs number of cycle, SL test, round specimens, testing frequency 15 Hz ($R = 0.1$)

- The thermal behavior of the specimens varied based on the applied stress amplitude levels: a stable horizontal trend for stresses below the fatigue limit, a decreasing trend slightly above the fatigue limit, and an increasing trend at higher stress levels. This phenomena provide critical insights into the material behavior under varying stress conditions.
- The application of the SL technique for data interpretation has suggests the potential of SL testing method for future fatigue resistance estimation improvement.
- The presented models and their respective error values provide a quantitative perspective of fatigue resistance estimation. This allows for more precise interpretations and predictions concerning the material fatigue behavior.
- Surface roughness, density measurements, and microstructural examination have revealed detailed insights into the intrinsic properties of the material, emphasizing the role of the PBF-LB/M method in influencing these characteristics.
- The material behavior under cyclic loading, as observed in the fatigue tests, provides valuable information for industries and applications where 316L stainless steel is pivotal.
- The correlation between thermal behavior, stress levels, and fatigue limits offers a holistic understanding of the material's response under varying conditions.

The broader implications of this study highlight the importance of the PBF-LB/M method in producing 316L stainless steel specimens with distinct properties. These findings can guide future research endeavors, pushing the boundaries of material science and engineering.

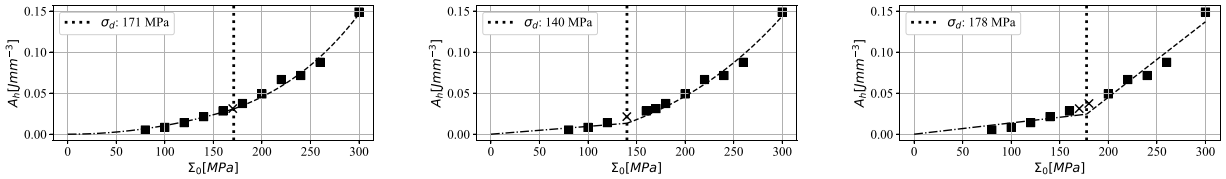

(a) Parabola Power law (b) Line below Power law (c) Line below Line

Fig. 15. Constant Amplitude Loading - Flat Specimen - hysteresis - R = −1.

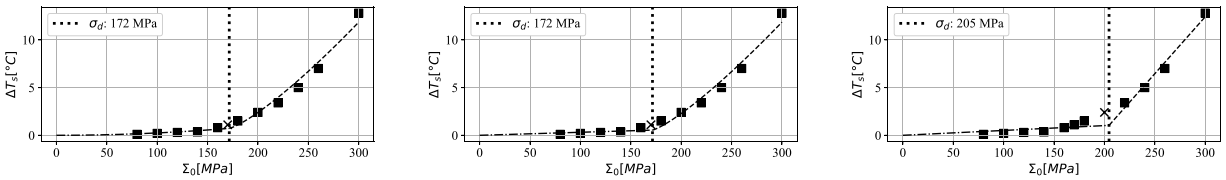

(a) Parabola Power law (b) Line below Power law (c) Line below Line

Fig. 16. Constant Amplitude Loading - Flat Specimen - Temperature increase - R = −1.

Comparing our findings with existing literature, the fatigue behavior observed for AM 316L aligns with general expectations for 316L stainless steel. However, nuances brought about by the PBF-LB/M method emphasize the importance of considering manufacturing techniques when studying material properties.

The implications of these results are wide, especially for industries reliant on 316L stainless steel. Understanding the material behavior under cyclic loading can help design decisions, ensuring product longevity and safety.

It would also be intriguing to investigate any anomalies or discrepancies observed during the experimental activity, delving deeper into potential causes and their implications. This could pave the way for further research and exploration in this domain.

Future research could delve deeper into optimizing the PBF-LB/M process parameters for improved fatigue performance or exploring the behavior of other materials using similar manufacturing techniques.

CRediT authorship contribution statement

Luca Santoro: Writing – original draft, Software, Methodology, Investigation, Data curation, Conceptualization. **Raffaella Sesana:** Writing – review & editing, Validation, Supervision, Conceptualization. **Johannes Diller:** Writing – original draft, Investigation. **Christina Radlbeck:** Writing – review & editing, Supervision. **Martin Mensinger:** Supervision, Resources.

Declaration of competing interest

The authors declare that they have no known competing financial interests or personal relationships that could have appeared to influence the work reported in this paper.

Data availability

No data was used for the research described in the article.

Appendix. Figure appendix

In the present section an overview of the result is presented. In the figure the experimental data are plotted, in particular the one used during the fitting of the optimal fatigue limit are plotted as (square), while the one excluded are plotted as (x). Then the optimal fatigue limit resulted from the iterative algorithm is presented as a vertical line (..), the curve fitted below the fatigue limit is presented as (-.) and the curve fitted above is presented as (–). Hence in the legend is presented the numerical value of the optimal fatigue limit (see Figs. 15–22).

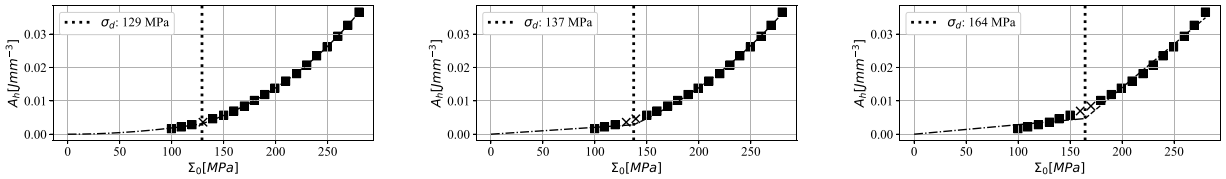

(a) Parabola Power law (b) Line below Power law (c) Line below Line

Fig. 17. Step Loading - Flat specimen - hysteresis - R = −1 - f =15 Hz.

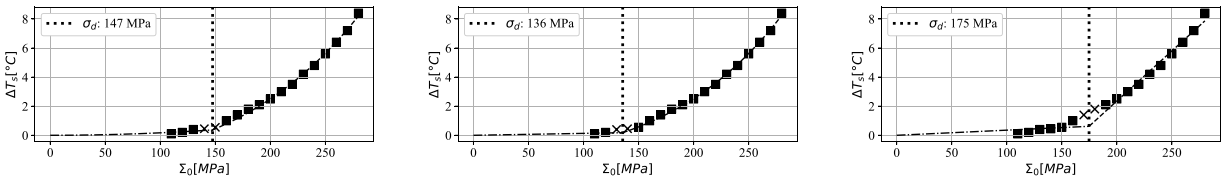

(a) Parabola Power law (b) Line below Power law (c) Line below Line

Fig. 18. Step Loading - Flat specimen - hysteresis - R = −1 - f = 15 Hz.

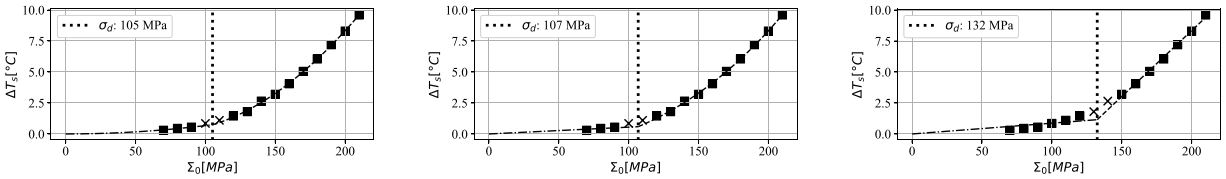

(a) Parabola Power law (b) Line below Power law (c) Line below Line

Fig. 19. Step Loading - Flat specimen - Temperature increase - R = −1 - f = 45 Hz.

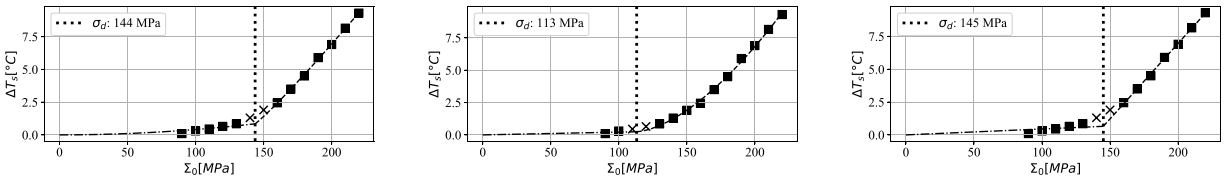

(a) Parabola Power law (b) Line below Power law (c) Line below Line

Fig. 20. Step Loading - Round Specimen no.1 - Temperature Increase - R = 0.1.

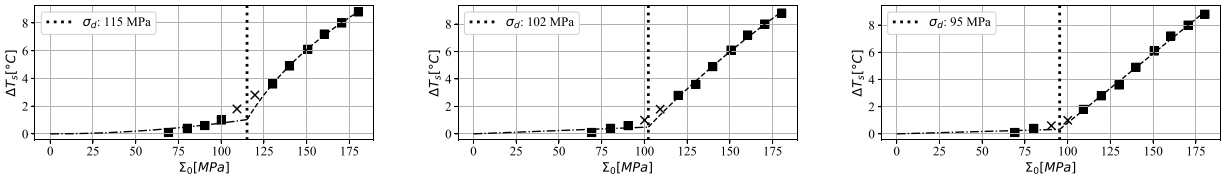

(a) Parabola Power law (b) Line below Power law (c) Line below Line

Fig. 21. Step Loading - Round Specimen no.2 - Temperature Increase - R = 0.1.

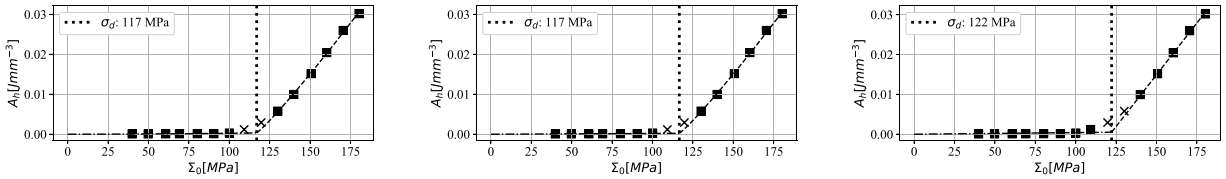

(a) Parabola Power law (b) Line below Power law (c) Line below Line

Fig. 22. Step Loading - Round Specimen no.2 - hysteresis - R = 0.1.

References

[1] B.J. Lazan, Damping studies in materials science and materials engineering, Intern. Frict. Damping Cycl. Plast. (1965) 1–20, http://dx.doi.org/10.1520/stp43762s.

[2] E. Charkaluk, A. Constantinescu, Dissipative aspects in high cycle fatigue, Mech. Mater. 41 (5) (2009) 483–494.

[3] N. Connesson, F. Maquin, F. Pierron, Dissipative energy as an indicator of material microstructural evolution, EPJ Web Conf. 6 (2010) 38013, http://dx.doi.org/10.1051/epjconf/20100638013.

[4] F. Maquin, F. Pierron, Heat dissipation measurements in low stress cyclic loading of metallic materials: From internal friction to micro-plasticity, Mech. Mater. 41 (8) (2009) 928–942, http://dx.doi.org/10.1016/j.mechmat.2009.03.003, URL: https://www.sciencedirect.com/science/article/pii/S0167663609000696.

[5] A. Chrysochoos, H. Louche, An infrared image processing to analyse the calorific effects accompanying strain localisation, Internat. J. Engrg. Sci. 38 (16) (2000) 1759–1788, http://dx.doi.org/10.1016/S0020-7225(00)00002-1, URL: https://www.sciencedirect.com/science/article/pii/S0020722500000021.

[6] R.E. Reed-Hill, R. Abbaschian, R.E. Reed-Hill, Physical metallurgy principles / Robert E. Reed-Hill, Reza Abbaschian, in: Physical Metallurgy Principles, third ed., in: <<The>> PWS series in engineering, PWS, Boston, 2008.

[7] R.S. Botny, J. Kaleta, W. Grzebień, W. Adamczewski, A method for determining the heat energy of the fatigue process in metals under uniaxial stress. Part 2. Measurement of the temperature of a fatigue specimen by means of thermovision camera-computer system, Int. J. Fatigue 8 (1) (1986a) 35–38, http://dx.doi.org/10.1016/0142-1123(86)90045-9.

[8] R.S. Botny, J. Kaleta, W. Grzebień, W. Adamczewski, A method for determining the heat energy of the fatigue process in metals under uniaxial stress. Part 2. Measurement of the temperature of a fatigue specimen by means of thermovision camera-computer system, Int. J. Fatigue 8 (1) (1986b) 35–38, http://dx.doi.org/10.1016/0142-1123(86)90045-9.

[9] N.R. Hansen, H.L. Schreyer, A thermodynamically consistent framework for theories of elastoplasticity coupled with damage, Int. J. Solids Struct. 31 (3) (1994) 359–389.

[10] F. Curà, A.E. Gallinatti, R. Sesana, Dissipative aspects in thermographic methods, Fatigue Fract. Eng. Mater. Struct. 35 (12) (2012) 1133–1147, http://dx.doi.org/10.1111/j.1460-2695.2012.01701.x.

[11] F. Curà, R. Sesana, Mechanical and thermal parameters for high-cycle fatigue characterization in commercial steels, Fatigue Fract. Eng. Mater. Struct. 37 (8) (2014) 883–896, http://dx.doi.org/10.1111/ffe.12151.

[12] F. Curà, G. Curti, R. Sesana, A new iteration method for the thermographic determination of fatigue limit in steels, Int. J. Fatigue 27 (4) (2005) 453–459, http://dx.doi.org/10.1016/j.ijfatigue.2003.12.009, URL: www.elsevier.com/locate/ijfatigue.

[13] R. Zu, Y. Zhu, X. Huang, Y. Huang, Y. Zhou, J. Zhao, Z. Liu, A fatigue limit evaluation method based on plastic strain incremental energy dissipation theory, Eng. Fract. Mech. 282 (2023) 109173, http://dx.doi.org/10.1016/j.engfracmech.2023.109173.

[14] A. Zhao, J. Xie, Y. Zhao, C. Liu, J. Zhu, G. Qian, S. Wang, Y. Hong, Fatigue limit evaluation via infrared thermography for a high strength steel with two strength levels, Eng. Fract. Mech. 268 (2022) 108460, http://dx.doi.org/10.1016/j.engfracmech.2022.108460.

[15] R. Munier, C. Doudard, S. Calloch, B. Weber, Determination of high cycle fatigue properties of a wide range of steel sheet grades from self-heating measurements, Int. J. Fatigue 63 (2014) 46–61.

[16] Q. Pierron, H. Maitournam, I. Raoult, Thermographic approach for high cycle fatigue of seam welded steel joints under variable amplitude loadings, Fatigue Fract. Eng. Mater. Struct. 43 (12) (2020) 2966–2983, http://dx.doi.org/10.1111/ffe.13348, https://onlinelibrary-wiley-com.ezproxy.biblio.polito.it/doi/full/10.1111/ffe.13348https://onlinelibrary-wiley-com.ezproxy.biblio.polito.it/doi/abs/10.1111/ffe.13348https://onlinelibrary-wiley-com.ezproxy.biblio.polito.it/doi/10.1111/ffe.13348.

[17] J.J. Faria, L.G. Fonseca, A.R. de Faria, A. Cantisano, T.N. Cunha, H. Jahed, J. Montesano, Determination of the fatigue behavior of mechanical components through infrared thermography, Eng. Fail. Anal. 134 (2022) http://dx.doi.org/10.1016/j.engfailanal.2021.106018.

[18] J. Huang, M.L. Pastor, C. Garnier, X.J. Gong, A new model for fatigue life prediction based on infrared thermography and degradation process for CFRP composite laminates, Int. J. Fatigue 120 (2019) 87–95, http://dx.doi.org/10.1016/j.ijfatigue.2018.11.002.

[19] A.V. Gonchar, V.V. Mishakin, V.A. Klyushnikov, The effect of phase transformations induced by cyclic loading on the elastic properties and plastic hysteresis of austenitic stainless steel, Int. J. Fatigue 106 (2018) 153–158, http://dx.doi.org/10.1016/j.ijfatigue.2017.10.003.

[20] G. Meneghetti, Analysis of the fatigue strength of a stainless steel based on the energy dissipation, Int. J. Fatigue 29 (1) (2007) 81–94.

[21] G. Meneghetti, M. Ricotta, B. Atzori, A synthesis of the push-pull fatigue behaviour of plain and notched stainless steel specimens by using the specific heat loss, Fatigue Fract. Eng. Mater. Struct. 36 (12) (2013) 1306–1322, http://dx.doi.org/10.1111/ffe.12071, URL: https://onlinelibrary.wiley.com/doi/abs/10.1111/ffe.12071.

[22] G. Meneghetti, M. Ricotta, The use of the specific heat loss to analyse the low- and high-cycle fatigue behaviour of plain and notched specimens made of a stainless steel, Eng. Fract. Mech. 81 (2012a) 2–16.

[23] D. Rigon, F. Berto, G. Meneghetti, Estimating the multiaxial fatigue behaviour of C45 steel specimens by using the energy dissipation, Int. J. Fatigue 151 (2021) 106381.

[24] C. Doudard, S. Calloch, F. Hild, P. Cugy, A. Galtier, Identification of the scatter in high cycle fatigue from temperature measurements, Comptes Rendus Mécanique 332 (10) (2004b) 795–801.

[25] C. Doudard, S. Calloch, P. Cugy, A. Galtier, F. Hild, A probabilistic two-scale model for high-cycle fatigue life predictions, Fatigue Fract. Eng. Mater. Struct. 28 (3) (2005) 279–288, http://dx.doi.org/10.1111/j.1460-2695.2005.00854.x.

[26] B. Blinn, M. Klein, C. Gläßner, M. Smaga, J.C. Aurich, T. Beck, An investigation of the microstructure and fatigue behavior of additively manufactured AISI 316L stainless steel with regard to the influence of heat treatment, Metals 8 (4) (2018) http://dx.doi.org/10.3390/met8040220.

[27] C. Douellou, X. Balandraud, E. Duc, B. Verquin, F. Lefebvre, F. Sar, Fast fatigue characterization by infrared thermography for additive manufacturing, Procedia Struct. Integr. 19 (2019) 90–100, http://dx.doi.org/10.1016/j.prostr.2019.12.011.
[28] R. Giovannozzi, Costruzione di macchine / Renato Giovannozzi, Pá'tron, Bologna, c1958-64.
[29] B. Lazan, Damping of materials and members in structural mechanics, Elsevier Science & Technology, 1968, URL: https://books.google.it/books?id=1qFRAAAAMAAJ.
[30] A. Järvenpää, L.P. Karjalainen, M. Jaskari, Effect of grain size on fatigue behavior of type 301ln stainless steel, Int. J. Fatigue 65 (2014) 93–98, http://dx.doi.org/10.1016/j.ijfatigue.2013.05.012.
[31] A. Di Schino, J. Kenny, Grain size dependence of the fatigue behaviour of a ultrafine-grained AISI 304 stainless steel, Mater. Lett. 57 (21) (2003) 3182–3185, http://dx.doi.org/10.1016/s0167-577x(03)00021-1.
[32] A. Hamada, L. Karjalainen, High-cycle fatigue behavior of ultrafine-grained austenitic stainless and TWIP steels, Mater. Sci. Eng. A 527 (21–22) (2010) 5715–5722, http://dx.doi.org/10.1016/j.msea.2010.05.035.
[33] J. Liu, X. Deng, L. Huang, Z. Wang, High-cycle fatigue behavior of 18cr-8Ni austenitic stainless steels with grains ranging from nano/ultrafine-size to coarse, Mater. Sci. Eng. A 733 (2018) 128–136, http://dx.doi.org/10.1016/j.msea.2018.07.043.
[34] ASTM-E466, Practice for conducting force controlled constant amplitude axial fatigue tests of metallic materials, 2021, http://dx.doi.org/10.1520/e0466-21.
[35] B. Zhao, J. Song, L. Xie, Z. Hu, J. Chen, Surface roughness effect on fatigue strength of aluminum alloy using revised stress field intensity approach, Sci. Rep. 11 (1) (2021) 1–17, http://dx.doi.org/10.1038/s41598-021-98858-0.
[36] J. Diller, J. Blankenhagen, D. Siebert, C. Radlbeck, M. Mensinger, Combined effect of surface treatment and heat treatment on the fatigue properties of AISI 316L, manufactured by powder bed fusion of metals using a laser (PBF-LB/M), Int. J. Fatigue 178 (2024) 108025, http://dx.doi.org/10.1016/J.IJFATIGUE.2023.108025, URL: https://linkinghub.elsevier.com/retrieve/pii/S0142112323005261.
[37] Y. Murakami, Effect of surface roughness on fatigue strength, in: Metal Fatigue, Elsevier Ltd, 2002, pp. 305–320, http://dx.doi.org/10.1016/b978-008044064-4/50016-5.
[38] Y. Murakami, T. Takagi, K. Wada, H. Matsunaga, Essential structure of S-N curve: Prediction of fatigue life and fatigue limit of defective materials and nature of scatter, Int. J. Fatigue 146 (2021) 106138, http://dx.doi.org/10.1016/j.ijfatigue.2020.106138.
[39] Y. Murakami, H. Masuo, Y. Tanaka, M. Nakatani, Defect analysis for additively manufactured materials in fatigue from the viewpoint of quality control and statistics of extremes, in: Procedia Structural Integrity, 19, 2019, pp. 113–122, http://dx.doi.org/10.1016/j.prostr.2019.12.014, URL: www.sciencedirect.com.
[40] D. Skibicki, A. Lipski, Pejkowski, Evaluation of plastic strain work and multiaxial fatigue life in CuZn37 alloy by means of thermography method and energy-based approaches of Ellyin and Garud, Fatigue Fract. Eng. Mater. Struct. 41 (12) (2018) 2541–2556, http://dx.doi.org/10.1111/ffe.12854.
[41] C. Doudard, S. Calloch, F. Hild, P. Cugy, A. Galtier, Identification de la dispersion des limites d'endurance à l'aide d'un essai d'échauffement, Comptes Rendus - Mecanique 332 (10) (2004a) 795–801, http://dx.doi.org/10.1016/j.crme.2004.06.002.
[42] D.L. Wenzler, K. Bergmeier, S. Baehr, J. Diller, M.F. Zaeh, A novel methodology for the thermographic cooling rate measurement during powder bed fusion of metals using a laser beam, Integr. Mater. Manuf. Innov. 12 (1) (2023) 41–51, http://dx.doi.org/10.1007/s40192-023-00291-w.
[43] N. Petch, The cleavage strength of polycrystals, J. Iron Steel Inst. 174 (1953) 25–28.
[44] G. Meneghetti, M. Ricotta, The use of the specific heat loss to analyse the low- and high-cycle fatigue behaviour of plain and notched specimens made of a stainless steel, Eng. Fract. Mech. 81 (2012b) 2–16, http://dx.doi.org/10.1016/j.engfracmech.2011.06.010.
[45] B. Vayssette, N. Saintier, C. Brugger, M. El May, E. Pessard, Numerical modelling of surface roughness effect on the fatigue behavior of Ti-6Al-4V obtained by additive manufacturing, Int. J. Fatigue 123 (2019) 180–195, http://dx.doi.org/10.1016/j.ijfatigue.2019.02.014.
[46] T. Boulanger, A. Chrysochoos, C. Mabru, A. Galtier, Calorimetric analysis of dissipative and thermoelastic effects associated with the fatigue behavior of steels, Int. J. Fatigue 26 (3) (2004) 221–229, http://dx.doi.org/10.1016/S0142-1123(03)00171-3.